

Design, Test and Optimization of Inductive Coupled Coils for Implantable Biomedical Devices

Jinwei Zhao, Rami Ghannam, Mengyao Yuan, Himmy Tam, Muhammad Imran, and Hadi Heidari*

School of Engineering, University of Glasgow, G12 8QQ, Glasgow, United Kingdom

(Received: 20 December 2018; Accepted: 10 February 2019)

Biomedical implant devices are fast becoming a growing part of the healthcare industry. Providing power to these devices in such a confined area is a critical challenge. Consequently, resonance-based wireless power delivery provides a harmless yet effective way for powering these implantable biomedical devices. This technique relies on transferring power via the inductive coupling technique. In this regard, optimizing the quality factor and matched resonant frequency is required to achieve high efficiency. However, the efficiency depends on the space available for the coil and the separation distance between the two coils. In our case, the minimum separation distance between the two coils needs to be at least 2 cm. Therefore, we demonstrate the design, simulation and experimental procedure of an optimized wireless power delivery system for bio-implantable applications with various considerations for size limitations. Our design delivers 68 mW output power to a 50-Ω load with an efficiency of 67% *in vitro* test and 74.8% in the FEM simulation.

Keywords: Implantable Electronics, Wireless Power Transfer (WPT), FEM Device Modelling, Coil Design, High-Efficiency Inductive Power Coupling.

IP: 130.209.12.71 On: Tue, 14 May 2019 10:49:29
 Copyright: American Scientific Publishers
 Delivered by Ingenta

1. INTRODUCTION

The application of implantable and wearable electronic devices is rising rapidly in modern medicine due largely to their capability of both real-time monitoring and stimulating organs locally.¹⁻⁴ The power supply in most conventional biomedical implant devices relies on batteries, which will require occasional surgical replacement or recharging via a transdermal or percutaneous approach. These procedures are either time-consuming or prone to infection. Emerging power harvesting and generation devices such as photovoltaic cells, piezoelectric generators or wireless power transfer (WPT) systems have previously been investigated in the literature.⁵⁻²⁰ There are several factors affecting the device performance and our ability to surgically implant these device under the skin, which mainly are: (1) size, (2) harvested (or delivered) power and (3) conversion efficiency.²¹ Table I shows a comparison between our work and other implantable power harvesting topologies in terms of the key factors mentioned above. The Piezoelectric Ultrasound Energy Harvester (PUEH) can deliver power at a long separation distance and enable small geometry of the implants.⁹ However, the amount of power is low (less 1 mW). In all energy

harvesting mechanism, heat is considered as “wasted” energy. However, Thermal Electric Generator (TEG) can be used to make use of this heat energy. They can be combined with other energy harvesting devices to detect difference in human body temperature.²² Photovoltaic (PV) cell can deliver high output power from a small area, which reduces system complexity in comparison to WPT and PUEU. Compared with other power harvesting methods, WPT is the only U.S. FDA (Food and Drug Administration) approved method.²³ The high conversion efficiency and power delivered makes it more and more applied in implantable devices.²³ However, short power transfer, tissue limitation, and complexity of tuning and circuitry are still huge challenges.²⁴ Near-Field Inductive Coupling method is the viable candidate for implantable power harvesting because it is easy to tune, advantageous of power delivered and higher efficiency.²³

Magnetically coupled resonant wireless power delivery systems consist of two coupled air-core coils, which act as a transmitter (primary) coil and a receiver (secondary) coil. When connecting an AC power source to the primary coil (outside of tissue), a time-varying magnetic field will induce a voltage in the secondary coil. To achieve maximum power delivery frequency, a strong magnetic field is required, which leads to considerable energy loss in addition to various safety problems.²⁵ There are a variety of

*Author to whom correspondence should be addressed.
 Email: Hadi.Heidari@glasgow.ac.uk

Table I. The implantable power harvesting methods comparison state of arts (primary coil, secondary coil).

Powering scheme	Size (mm)	Specifications	Power (mW)	Efficiency	Ref.
PUEG	L:0.7 W:0.7 T:1.4	1 MHz	0.18	50%	[17]
PUEG	L:1 W:1 T:1.4	1 MHz	0.36	50%	[17]
PV	L:1.3 W:1.3 T:1	Visible-NIR	25.4	20%	[9]
PV	L:2.7 W:3.3	NIR	3.44	27.7%	[10]
TEG	L:2.4 W:3.3 T:1.1	27 °C	0.15	N/A	[19]
TEG	D:9.3 T:1.4	20–25 °C	0.03	N/A	[19]
NFIC	D:(60, 25) T:(10, 5)	13.56 MHz	10	58.2%	[14]
NFIC	D:(30, 20)	8 MHz	68.7	63.9%	[16]
NFIC	D:(60, 20) T:(10, 2)	3.25 MHz	68	67%	This work

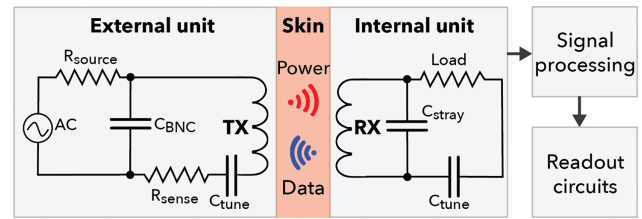
implantable applications that use WPT as the main source of power, such as cochlear implants, neurostimulators and cardiac pacemakers.²⁶

In fact, WPT can be achieved using three main methods: (1) Inductively Coupled Method (ICM); (2) Capacitively Coupled Method (CPM); and (3) Ultrasonic Power Transfer Method (UPM). Compared with other methods, the inductively coupled method enables the transfer of power outputs ranging from microwatts to several watts at relatively high efficiency in the near-field range.²⁶ The aim of this paper is twofold: (a) to demonstrate the size constraints of implantable near-field inductively coupled coils, and (b) report the optimized power delivery efficiency through human tissue, which is achieved by improving the quality factor and resonant matching frequency in the coil.

2. PRINCIPLES OF INDUCTIVE COIL

2.1. Near-Field Inductively Coupled Coils

Near-field inductive power transfer can be achieved if the coils are aligned in close proximity to one another. There are different coil technologies for WPT. For instance, the 2-coil, 3-coil and 4-coil systems are examples of multi-coil systems. Multi-coil systems enable greater power transfer efficiency and a larger separation distance between the coils. However, this is predominantly useful for small power delivery in the mid- and far-field frequency ranges.^{26–29} In our case, we adopt the 2-coil system due to its low cost, simple design, easy tuning and large power delivery.²⁷ However, to prevent tissue loss, we must ensure that our system transfers less than 100 mW through the body and that the operating frequency is much greater than 100 kHz.²³ Consequently, due to specific absorption rate (SAR) safety limits, our work focuses on the design and optimization of a 2-coil system that is operated in the MHz range, which will transfer 68 mW of power with 67% high efficiency.²³ As shown in Table I, increasing the operating frequency enables us to induce the coil geometry. However, the amount of declined power and the efficiency will also be reduced. The opposite is true if we reduce the operating frequency. Our design satisfies the required power

**Fig. 1.** The schematic of two-coil near-field inductively coupled power transfer system.

and SAR safety limits, while enabling a high efficiency and a more compact device size as shown in Table I.

The two-coil near-field inductive coupled system is shown in Figure 1. The transmitting and receiving coils can be regarded as two inductances coupled by a mutual inductance, M . Since the coils are resistive and due to stray capacitance, the losses attributed by these components cannot be ignored. The effect of these unwanted parameters can be predicted using COMSOL, which is a macroscopic finite element simulations tool. Thus, the power transfer can be optimized by changing the relative parameters of inductive coils. Impedance matching is one of the techniques for optimizing the output efficiency. Here, reactive power is always lagging in power transfer systems based on inductive coils. Thus, capacitors are used to compensate and reduce the reactive power in impedance matching, which will increase the transfer efficiency and stability of the system.

2.2. Numerical Analysis of kQ Product

Three major requirements must be fulfilled for achieving high power transfer efficiency. Firstly, the product of the Coupling Coefficient (k) and Quality Factor (Q) must be optimized. Secondly, the system must be operated at the appropriate resonant frequency. Finally, impedance matching is necessary to improve the power transmission efficiency when the quality is already optimal.

The transmission efficiency (η) can be determined using Eq. (1):^{26,30}

$$\eta_{\text{link}} = \frac{k^2 Q_1 Q_2}{(1 + \sqrt{1 + k^2 Q_1 Q_2})^2} \quad (1)$$

Consequently, the product of k and Q affect the magnitude of the power transmittance efficiency. The Coupling coefficient can be determined using:²⁶

$$k = \frac{M}{\sqrt{L_1 L_2}} \quad (2)$$

Where M is the mutual inductance between the two coils with inductance L_1 and L_2 , respectively. The k is normalized and can be compared in different coil geometries. Nevertheless, it is very hard to improve the value of k when the geometry is limited in some scenario, such as implantable application. In this case, increasing the value

of Q is the best way to increase the power transmittance efficiency.

The coil quality factor can be determined using Eq. (3):^{26, 29}

$$Q = \frac{\omega L_{\text{eff}}}{\text{ESR}} = \frac{2\pi L_{\text{eff}} \times (1 - f^2/f_{\text{self}}^2)}{R_{\text{dc}} \times (1 + f^2/f_h^2)} \quad (3)$$

where L_{eff} is effective inductance of the coil, f is the operating frequency, f_{self} is the coil's self-resonant frequency, f_h is the frequency at which active power is half of reactive power in the coil. L_{self} is the self-inductance and R_{DC} is the DC resistance of the coil. From Eq. (1), increasing the operating frequency improves the coil quality factor, which maximizes the power-transfer efficiency. However, when the operating frequency is increased to the coil's self-resonant frequency, the transmission efficiency drops to nearly zero. Since the coil turns are very close to each other, they suffer from parasitic capacitance.^{25, 29, 31–33} There are two types of parasitic capacitance in solenoid coil: (a) capacitance between turns (C_m) and (b) capacitance between turns (C_b). The parasitic capacitances in the coils can be determined using:²⁹

$$C_b = \varepsilon_0 \varepsilon_r \times \int_0^{\pi/4} \frac{\pi D_c R_w}{T + \varepsilon_r R_w (1 - \cos \theta)} d\theta \quad (4)$$

$$C_m = \varepsilon_0 \varepsilon_r \times \int_0^{\pi/4} \frac{\pi D_c R_w}{T + \varepsilon_r R_w (1 - \cos \theta) + 0.5 \varepsilon_r h} d\theta \quad (5)$$

Where ε_0 , ε_r are the permittivity of material, T is the thickness of coil, D_c is the diameter of the coil, R_w is the radius of wire and h is the separation between two layers. The total parasitic capacitance can be calculated using:^{29, 33}

$$C_{\text{self}} = \frac{1}{(N_t N_l)^2} \times \left[C_b (N_t - 1) N_l + C_m \sum_{i=1}^{N_l} (2i - 1)^2 (N_t - 1) \right] \quad (6)$$

Where N_t is the number of turns and N_l is number of layers. The analytical expression of self-inductance is:²⁹

$$L = \frac{N}{2} \mu_0 D_c \ln \left(\frac{D_c}{D_w} \right) \quad (7)$$

Where the μ_0 is permeability of vacuum, D_w is the diameter of a single turn and L_{eff} is the effective inductance related to frequency. The effective inductance is higher than the self-inductance at a low frequency, which is computed as:²⁹

$$L_{\text{eff}} = \frac{L}{1 - 4\pi^2 f^2 L C_{\text{self}}} \quad (8)$$

In essence, the coils can be approximated as a simple RLC circuit, as shown in Figure 1. When the operating frequency is higher than the self-resonant frequency, the coil behaves as a capacitor, which can only set up a very weak

magnetic field. The coil's self-resonant frequency (f_{self}) can be calculated using:²⁹

$$f_{\text{self}} = \frac{1}{2\pi \sqrt{L_{\text{self}} C_{\text{self}}}} \quad (9)$$

The coil's self-resonant frequency should be 3 or 4 times greater than the operating frequency to ensure the coil is still dominated by inductance. Since the coil design is both multi-turn and multi-layer solenoid coil, the power loss in the coil is predominantly caused by proximity effects rather than skin effect. Thus, f_h can be determined using:

$$f_h = \frac{2\sqrt{2}}{\pi r_s^2 \mu_0 \sigma \sqrt{N_t N_s \eta \beta}} \quad (10)$$

Where σ is the conductivity of the material, N_t is the number of turns, N_s is the number of strands, η and β are ratios related to coil geometry, r_s is the radius of strands.

Similarly, the mutual inductance, M is significantly dependent on k , as previously demonstrated in Eq. (2). The mutual inductance can also be determined using:³⁴

$$M_{12} = \frac{V_2}{j\omega I_1} \quad (11)$$

Where V_2 is the voltage between the secondary coil and I_1 is the current across the primary coil and ω is the angular frequency of the system.

In conclusion, the coil quality factor can be maximized by increasing the operating frequency to several megahertz and by using a greater number of turns, which increases the effective inductance. Increasing the inductance will decrease k , which results in a poorer link efficiency. In design procedure, it is always required to consider the trade-off point between k and Q . However, implantable biomedical devices suffer from coil size limitations, frequency limitation due to safety concerns. Consequently, the aim of this paper is to demonstrate the design process that is required in order to determine a coil geometry that yields optimal transmission efficiency.

3. DESIGN METHODOLOGY

The design procedure of the whole system is shown in Figure 2. The first step of the design process involves listing the design constraints based on the limitation of coil size. Next, we aim to achieve as many coil turns as possible for better quality factor. Next, we determine whether the coil's self-resonant frequency is higher than the operating frequency. This is the most important step, which ensures that the coil will still behave like an inductor when operating at that frequency. The coil's self-resonant frequency can be increased by using fewer turns and increasing the separation between the wires. When designing the primary coil, there are generally no limitations of the transmitter coil being placed *in vitro*.

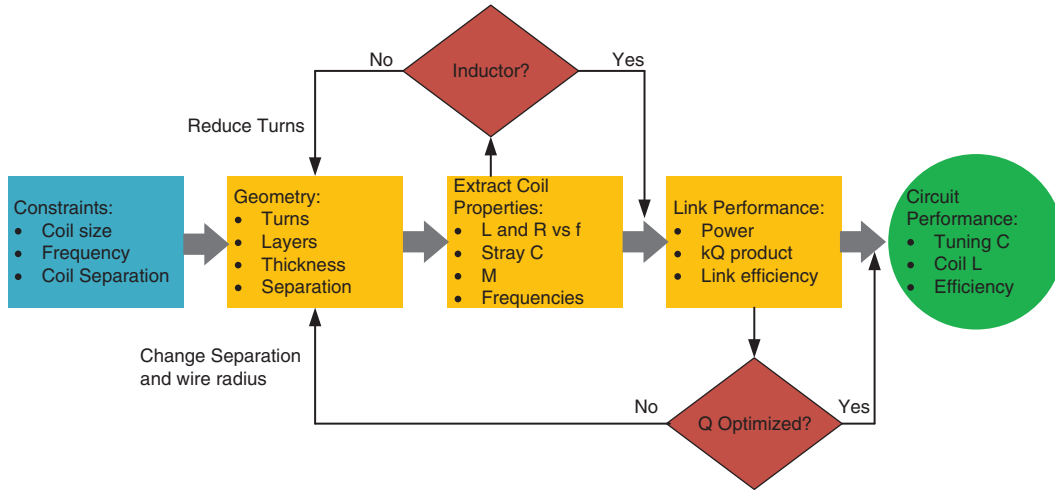


Fig. 2. The design procedure of implantable inductively coupled coils.

Based on the electromagnetic theory of a circular coil, the magnetic field strength between two coils can be determined using:³¹

$$H(x, r) = \frac{I_r^2}{2\sqrt{(r^2 + x^2)}} \quad (12)$$

where r is the coil radius, x is the separation between two coils and I_r is the magnitude of current. When the distance x is increased a weaker magnetic field will be experienced by another coil. Based on the design constraints summarized in Table II, the separation between the two coils will be 2 cm. To maximize the magnetic field strength that is experienced by the implantable coil, the radius of the primary coil should be the same as the distance separating the two coils multiplied by root 2. Therefore, the outer diameter of the coil is approximately 6 cm. After both coils have an acceptable quality factor a tuning capacitor should be connected to both coils, which will make both the primary and implantable coils resonate at the same frequency. The resonant frequency of the LC tank circuit can be determined using:²⁵

$$f = \frac{1}{2\pi\sqrt{LC_{\text{total}}}} \quad (13)$$

where L is the inductance of the coil, C is the total capacitance of the circuit. The inductance of the coil can be accurately determined by the LCR meter. C_{total} of the circuit

Table II. Design constrains.

Parameters	Design value
Receiver coil outer diameter	2 cm
Receiver coil thickness	0.20 cm
Transmitter coil outer diameter	6 cm
Operating frequency	3–5 MHz
Power delivered	Few mW

is the sum of the coil’s parasitic capacitance and the tuning capacitance. If the value of tuning capacitance is much higher than the parasitic capacitance, the effect of parasitic capacitance can be ignored. However, if the inductor has inductance within one hundred micros Henrys and is being tuned to resonate at a few megahertz, the parasitic capacitance will usually cause a resonant frequency shift and thus reduce the transmission efficiency at the desired operating frequency. Accurately determining the coil parasitic capacitance is important for boosting the transmission efficiency.

The total impedance of the primary coil circuit can be determined using:

$$Z_{\text{total}} = \left(R + j \left(\frac{\omega L}{1 - \omega^2 LC} - \frac{1}{\omega C_1} \right) \right) / \left(1 - \frac{\omega^2 LC_2}{1 - \omega^2 LC} + \frac{C_1}{C_2} + j\omega RC_2 \right) \quad (14)$$

At resonant frequency, the imaginary part of the impedance is equal to zero. Thus:

$$-(1 - \omega^2 LC)^2 \left(\omega^2 R^2 C_2 + \frac{1}{C_1} \left(1 + \frac{C_2}{C_1} \right) \right) + (1 - \omega^2 LC) \left(\omega^2 L + 2\omega^2 L \frac{C_2}{C_1} \right) - \omega^4 L^2 C_2 = 0 \quad (15)$$

where L, C, C_1, C_2 is the same component which shown as Figure 1. C_1 is the value of tune capacitor and C_2 is the BNC wire capacitance = 7.60 pF, which can be measured precisely. The only unknown parameter is the parasitic capacitance of the coil C . By placing different tuning capacitances, different resonant frequencies can be observed. In Eq. (13) is the resonant frequency $\times 2\pi$. By solving this equation with a different tuning capacitor and corresponding resonant frequency, the same root can be obtained. This is the parasitic capacitance. The resonant

frequency of the coil circuit when including the parasitic capacitance can be calculated as Eq. (16):

$$f_{\text{real}} = \frac{1}{2\pi\sqrt{C + C_1}} \quad (16)$$

And the comparison of measured resonant frequency to predicted one from Eq. (16) can be plotted as Figure 4. In addition, the coils are tested by powering through a piece of ham *in vitro* analysis, which is shown in Figure 3.

4. EXPERIMENTAL RESULTS AND COMPARISON

Our experimental results are compared with COMSOL simulations for verification purposes. The coil dimensions were shown in Table III. The simulation process is explained in greater detail in Section 5. Firstly, the coil is wound by the winding machine precisely. The primary coil currently contains 35 turns only and the coil size is slightly smaller. The real coils are shown in Figure 3. The coil parameters such as inductance, resistance and parasitic capacitance can be measured by LCR Meter, while the capacitance is difficult to test because the meter yield nonsensical reading and the parameter capacitance is too small in picofarad scale. The coil properties are shown in Table IV with a frequency of 3.25 MHz.

Secondly, the impedance matching is necessary to compensate the reactive power in the circuit. The series connection method is utilized because the series connection

Table III. The coil geometry that yield optimal quality factor.

Parameters	Primary coil	Secondary coil
Coil diameter	6 cm	2 cm
Wire radius	0.10 mm	0.05 mm
Total number of turns	35	40
Turns per layer	35	20
Number of layers	1	2

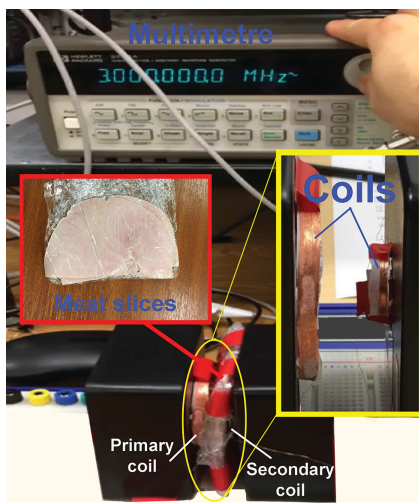


Fig. 3. The *in-vitro* test of near-field power transfer system.

Table IV. The coil properties at 3.25 MHz compared between simulation (*S*) and measurement (*M*).

Parameters	Primary coil	Secondary coil
Inductance (<i>M</i>)	141.36 μH	58.42 μH
Inductance (<i>S</i>)	137.06 μH	52.65 μH
Resistance (<i>M</i>)	5.60 Ω	6.68 Ω
Resistance (<i>S</i>)	3.50 Ω	5.33 Ω
Quality factor (<i>M</i>)	750	230
Quality factor (<i>S</i>)	761.10	167.77

is advantageous in both weakly coupling and strong coupling. Compared to the series connection method, the parallel connection topology suffers from strong coupling regime. The capacitors applied in our circuit are shown in Figure 4. The analytical solution is simulated by MATLAB using Eq. (13). The magnitude of the tuning capacitor cannot be an arbitrary value, since it depends on its market value. As previously mentioned, with the exception of the capacitance, the inductance and resistance of the coil can be clearly measured by an LCR meter. Three capacitors are involved in the system, which potentially influences the value of self-resonant frequency. The capacitance of the BNC wire is from 7.60 pF to 130 pF in the instrumentation, which did not cause any noticeable resonant frequency effect, which means that it can be neglected. Equation (16) is included to solve self-resonant frequency mismatch. The analytical solution is perfectly matched with real-circuit measurement. Thus, it is obvious the Eq. (16) is improved the capacitor approximation compared with Eq. (13) in real circuit design. As all the steps are completed, the power transmission efficiency can be achieved, which is shown in Figure 5. The data from the measurement is triggered by applying the “curve fitting” tool in Matlab. The efficiency from the simulation is slightly higher than the measurement result because the heating loss from the instrument. The main reason

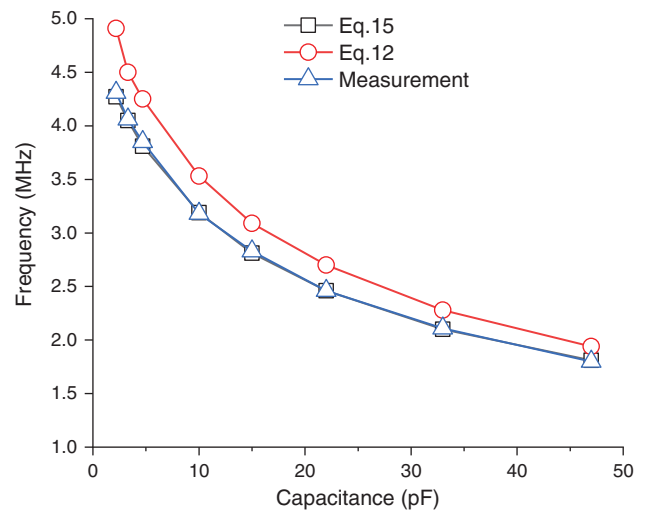


Fig. 4. The resonant frequency as a function of tuning capacitor. The predicted (Eq. (15)) and experimental results show the good agreement.

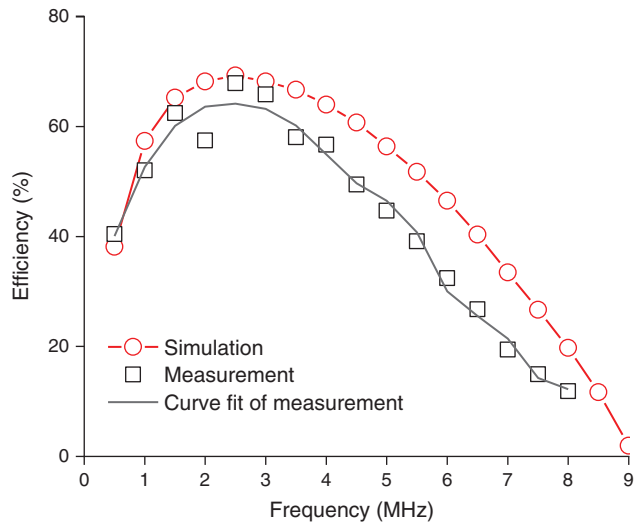


Fig. 5. The comparison between COMSOL simulation and experimental result for the power transmission efficiency.

is the self-resonant capacitance because the value is not evaluable in measurement and difficult to simulate the frequency-dependent capacitance accurately.

The transmission efficiency is determined by the power delivered to the 50-Ohm secondary resistor divided by the input power in the primary side. A 0.5 cm thick chunk of ham was used to imitate human tissue while the receiver coil was covered. With the high coil quality factor and accurate resonant frequency prediction, the two coil systems with the structure mentioned in Table IV can achieve around 67% of transmission efficiency when the relative distance is 2 cm at 3.28 MHz. A total of 68 mW can be delivered to the load resistor which meets the power requirement of delivering about few tens' mW for the implantable device.¹¹ In this experiment, the tissue is nearly transparent to the system. As the permeability of tissue is close to the free space, the inductance of the coil remains unchanged. As the resonant frequency is

selected to be lower than 4 MHz, the capacitance of tuning capacitor is much higher than the parasitic capacitance contributed by the tissue, thus the tissue effect becomes minuscule.

5. FEM SIMULATION AND DEVICE OPTIMIZATION

COMSOL was used for simulating the magnetic field distribution and magnetic resonance between the coils. The coil model was developed in the 2D axisymmetric formulation. 3D simulations were also developed to show the magnetic field distribution. Since the processing time of 2D simulations is considerably less than 3D, 2D simulations were used to process important calculations such as parameter sweep. The axisymmetric principle in 2D modelling is shown in Figure 6. A circle (sphere in 3D) with a diameter of 15 cm is aligned as the FEM magnetic field boundary, which means that only the objects inside the circle will be analyzed otherwise will be neglect. The material of the circle is aligned with air, and the coils' material is set up with copper. Now turning point to the geometry of the coils, the geometry parameters are set up as same as experimental works. According to the design constraint, the separation distance between two coils is less than 2 cm, where the distance is regarded as the length between the circle's centers of two coils. Next, the Magnetic Field Physics is added in the model to set up the magnetic to the electrical interface. It is based on the Ampere's Law, and the magnetic boundary is set up by the sub-section called Magnetic Insulation. The initial condition is set by a standstill magnetic field, where the magnetic vector potential is zero at x -, y - and z -axis respectively. The operational temperature is set to room temperature 293.15 K, and some material properties such as conductivity permittivity and permeability are aligned to the built-in material: air (Ciddor) and copper (AC-DC). The sub-module called Coil ports are involved in exciting the transmitter coil and receiver coil. The relative parameters are utilized

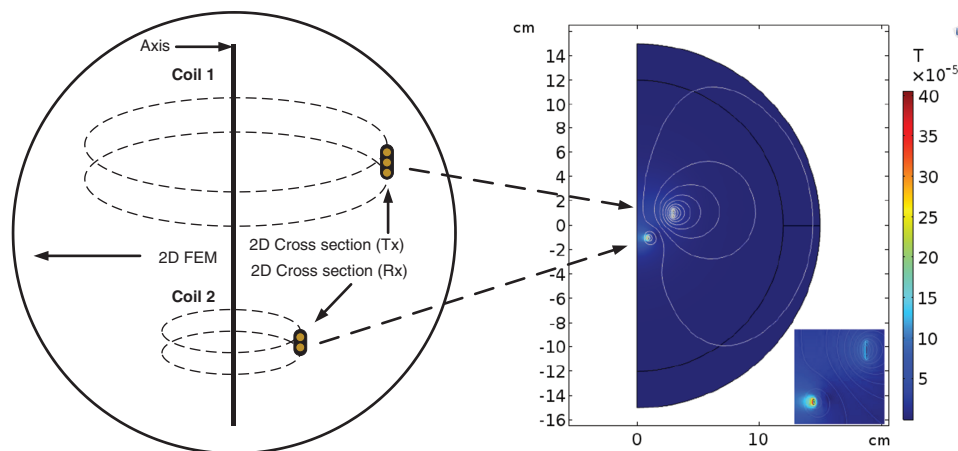


Fig. 6. The 2D axisymmetric model of the 2-coil near-field inductively coupled power transfer system, which was simulated using COMSOL.

in this setting, such as turns number, conductivity, cross-section area of the coil. Moreover, the conductor model is set to Homogenize multi-turn coil and the coil can be excited by voltage, current and power. The self-inductance can be determined by exciting a coil with a current, which can be instrumented by the software automatically. The relative results can be achieved when the sending coil is supplied with 30 mA AC current, the receiving is induced and supply a 50 ohms resistor by involving electrical circuit physics in AC-DC module. The quality factor of the primary coil and the secondary coil are shown in Figures 7(a) and (b), which vary with the turns per layer.

With the turn numbers rise, the inductance of coil rises according to the Eq. (7) because of the product of C_{self} , L_{eff} and ω are much smaller than 1. With the increase of turn numbers, the self-resonant frequency is decreased

because the inductance is increased. The stray capacitance is decreased with higher frequency. With the self-resonant degrading, the quality will meet a trade-off point where the maximum quality factor is achieved. The maximum quality factor for the primary coil is 1480 with 160 turns, while the one for the secondary coil is 380 with 35 turns. According to the turn numbers, it is easy to find out the relative self-resonant frequency of both coils. Where the parameter values of the optimized coil can be obtained, which is $L_1 = 2.30 \mu\text{H}$, $C_1 = 0.10 \text{ pF}$ and $L_2 = 164.10 \mu\text{H}$, $C_2 = 6.50 \text{ pF}$. As it is an implantable device, the dimensions of the coils are required to be considered, where the thickness of the primary coil is 1.64 cm, the thickness of the secondary coil is 0.17 cm. The width of the coils can be only achieved if the number of layers can be determined, which will be shown in the next step. The f_h also affect the magnitude of quality factor in Eq. (3)

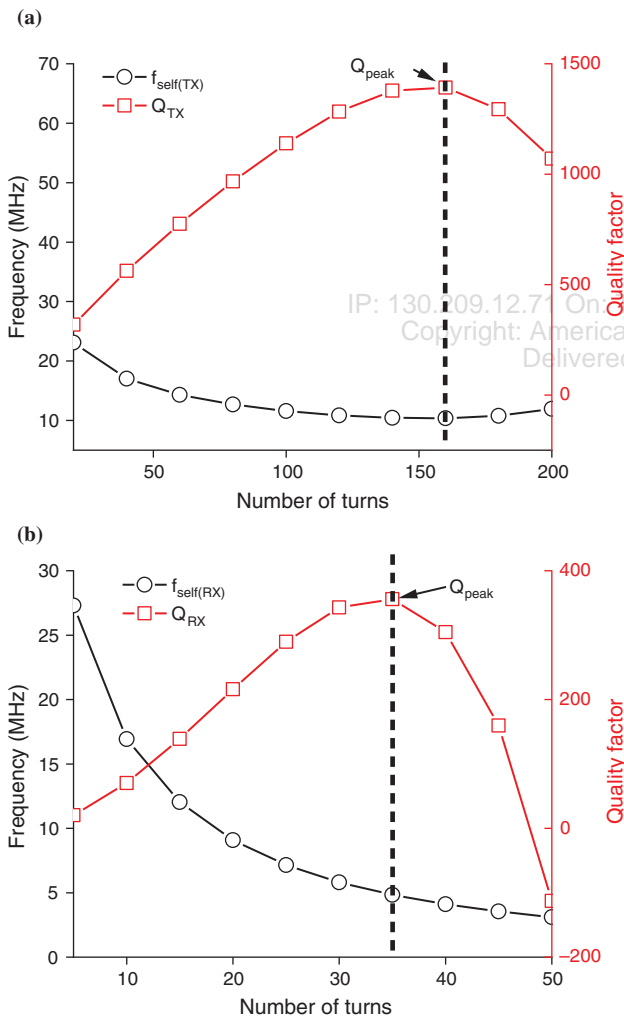


Fig. 7. Quality factor optimization by sweeping number of turns. (a) Quality factor and self-resonance frequency of primary coil according to number of turns (b) quality factor and self-resonance frequency of secondary coil according to number of turns. The number of turns is defined by the maximum quality factor point, which are 160 (primary coil) and 35 (secondary coil) respectively.

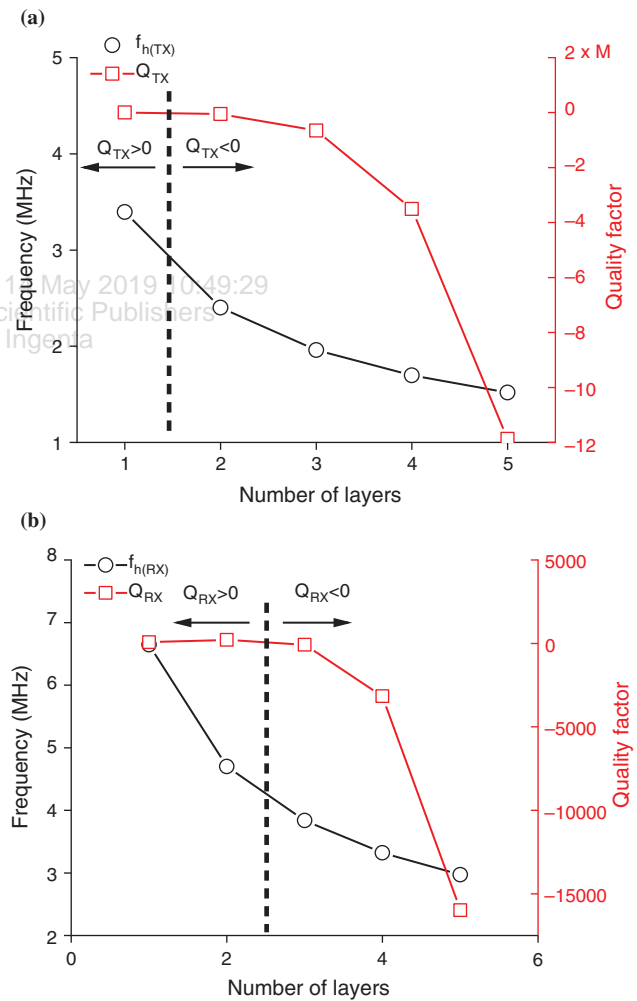


Fig. 8. Quality factor optimization by sweeping number of layers. (a) The quality factor and half-power frequency of primary coil according to number of layers. (b) The quality factor and half-power frequency of secondary coil according to number of layers. The dashed line indicates the number of layers for primary coil and secondary coil, which are 1 and 2 respectively.

and it can be optimized by changing layer numbers shown in Figures 8(a) and (b). For a great inductive coupling coil, a large value of f_h is always required, which means the change in coil AC resistance according to the proximity effect and the skin effect is not changed rapidly with the frequency increased. The dashed lines in Figures 8(a) and (b) provide the maximum layers for the coils because the quality factor cannot less than 0, which are 1 layer for the primary coil and 2 layers for the secondary coil. However, the layer should be as small as possible, since the quality factor is inversely proportional to the number of layers. The self-resonant frequency is slightly influenced by layer numbers, but the change is only a 1% difference between one layer and two layers. As the half power frequency is achieved, it is easy to obtain the AC resistance.

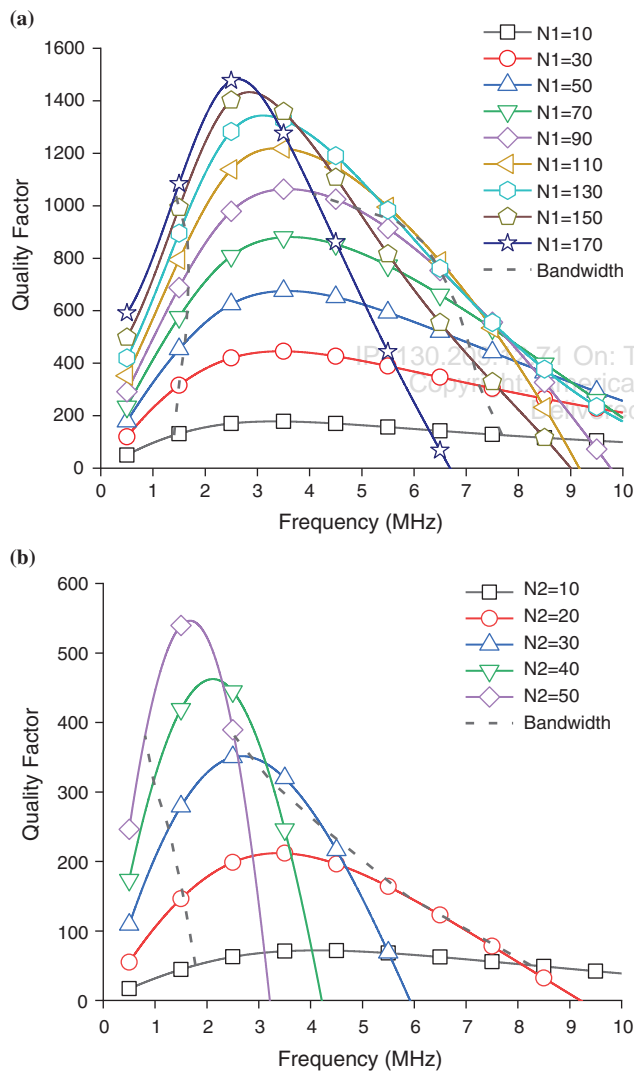


Fig. 9. The quality factor and bandwidth with different turn numbers. (a) The quality factor and half-power frequency of primary coil versus frequency for different turn numbers. (b) The quality factor and half-power frequency of secondary coil versus frequency changes and swept by different turn numbers. The band gap becomes narrowed as the number of turns increases.

For instance, the Resistance for 1-layer primary coil at 3.25 MHz is 6.72 Ohms, and 1-layer secondary coil at the same frequency is 5.34 Ohms. The bandwidth of inductive coil is also essential for the quality of designs, which regulates the range of operational frequency. To obtain the bandwidth and compare between the different number of turns, it is necessary to sweep the relative parameters, where the results are shown in Figures 9(a) and (b). It is clear to see that the bandwidth starts rapidly narrowed when the turn numbers are greater than a threshold value. This phenomenon appears when the number of turns of primary and secondary coils are higher than 130 and 10 respectively. It is always necessary to guarantee the bandwidth greater than the operational frequency. Due to the constraints (3–5 MHz), the turns number of secondary coils are limited below 30.

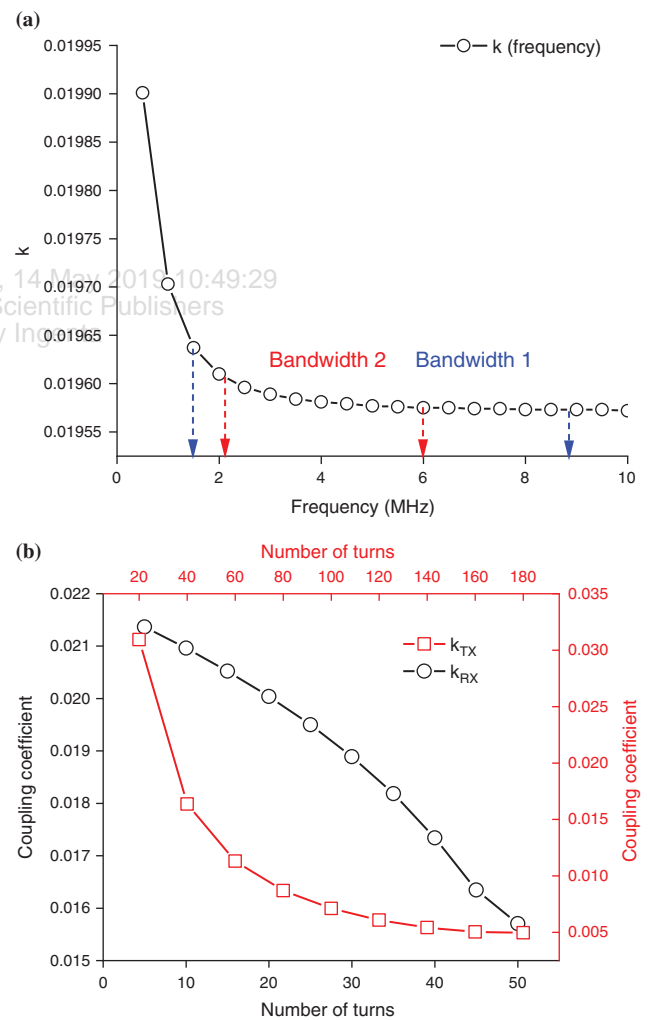


Fig. 10. The coupling coefficient optimization. (a) The coupling coefficient according to the operation frequency. (b) Coupling coefficient according to primary coil number of turns (k_{TX}) and secondary coil number of turns (k_{RX}). Increase the number of turns and operating frequency, degrade the coupling coefficient.

Table V. Ideal design based on FEM simulation.

Parameters	Primary coil	Secondary coil
kQ product	9.84	6.47
Turn numbers	20	30
Layer numbers	1	2
Diameter (cm)	6.04	2.02
Thickness (cm)	0.4	0.2
Inductance (μH)	60.93	126.65
Capacitance (pF)	0.78	5.94
Resistance (Ω)	2.00	10.67

Now turning point to the coupling coefficient, it varies with the operational frequency, number of turns, number of layers and distance between two coils. First, the influence of layers numbers can be neglected, because the primary coil is fixed at 1, and 3% difference between 2-layer and 1-layer secondary coil (0.0196 and 0.0190 respectively). Secondly, the effect from the various distance can be neglected as well, because the distances for the implantable devices are limited. The k over operational frequency is shown in Figure 10(a), and the coupling coefficients of the primary coil and secondary coil over the number of turns are shown in Figure 10(b). Based on the bandwidth in the previous analysis, the coefficient varies only with 1.50% difference. Thus, the effect due to operation frequency can be also neglected. There are significant changes of coefficient when the number of turns is changed. To be specific, the coupling coefficient of primary coil drops from 0.0315 to 0.005 when the turn number is increased up to 180, while the one for secondary coil decreases from 0.0215 to 0.0158 when the turn number rise to 50. In this case, the Quality factor itself cannot

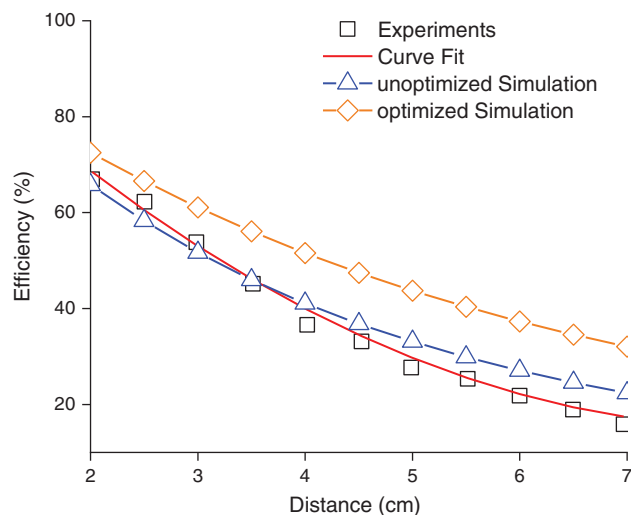


Fig. 11. The variation of efficiency according to different separation distances. The experimental data was evaluated from the *in-vitro* test in Section 4, and the data was refined using the built-in curve fit tool in MATLAB. The unoptimized simulation is developed using COMSOL with the same experimental setup in Section 4. The optimized simulation is built up with the coil properties in Section 5.

indicate how good the design, and a kQ product needs to be involved. The value can be achieved by multiplying the data in Figures 7 and 8 properly. The final optimized design is shown in Table V. With this design, efficiency of 74.8% can be finally achieved, which is improved by 7.80% compared with the initial design. However, this is an ideal design from the simulation, the practical results also depend on some technical conditions, such as the coil separations in the winding, the gap between the strands. The efficiency variation due to separation distance is shown in Figure 11. This shows the experimented simulation results of an unoptimized WPT system. Similarly, we have used these experiment results to develop a COMSOL simulation program that enabled us to optimize a WPT system. The optimized system obtained a 74.8% maximum conversion efficiency at 2 cm as mentioned above. With the distance increased, the flux linkage between two coils was degraded. This makes the conversion efficiency and power transfer capability diminished.²³ The separation distance is always constrained by the implantable applications in practice.²³

6. CONCLUSION

This paper demonstrated a highly efficient WPT system design and determined its constraints. The iterative design procedure discussed in Figure 2 enabled to improve the performance of a WPT system in implantable applications. The experimentally achieved transmission efficiency of 67% at 3.28 MHz. Moreover, 68 mW of power were delivered to the secondary coil when the relative distance between the coils is 2 cm. 68 mW power delivered can easily drive implants with massive consumption, such as cochlear hearing aids. Device optimization was achieved using COMSOL, which was used to obtain an improved efficiency reaching 74.8%.

An advanced WPT system requires additional component to convert and manage the harvested energy in order to power the load. For example, we need DC-AC, AC-DC and DC-DC converter. Moreover, implantable sensors produce reactive power. Consequently, in order to optimize the design of a WPT system, we will need to consider these components in addition to the reactive power produced by implantable sensors. These issues will be investigated and reported in our next publication.

Acknowledgment: This work was supported by the Royal Society under grant RSG\R1\180269 and UK Engineering and Physical Sciences Research Council (EPSRC) under grant EP/R511705/1.

References

1. H. Li, A. Shrestha, H. Heidari, J. Le Kernec, and F. Fioranelli, A multisensory approach for remote health monitoring of older people. *IEEE Journal of Electromagnetics, RF and Microwaves in Medicine and Biology* 2, 102 (2018).

2. N. Alduais, J. Abdullah, A. Jamil, and H. Heidari, Performance evaluation of real-time multivariate data reduction models for adaptive-threshold in wireless sensor networks. *IEEE Sensors Letters* 1, 1 (2017).
3. X. Liang, R. Ghannam, and H. Heidari, Wrist-worn gesture sensing with wearable intelligence. *IEEE Sens. J.* 19, 1082 (2018).
4. K. O. Htet, H. Fan, and H. Heidari, Switched capacitor DC–DC converter for miniaturised wearable systems, *IEEE Int. Symposium on Circuits and Systems (ISCAS)* (2018), pp. 1–5.
5. S. Wen, H. Heidari, A. Vilouras, and R. Dahiya, A wearable fabric-based RFID skin temperature monitoring patch. *2016 IEEE Sensor* (2016), pp. 1–3.
6. K. Oo Htet, R. Ghannam, Q. H. Abbasi, and H. Heidari, Power management using photovoltaic cells for implantable devices. *IEEE Access* 6, 42156 (2018).
7. K. O. Htet, J. Zhao, R. Ghannam, and H. Heidari, Energy-efficient start-up power management for batteryless biomedical implant devices. *IEEE Int. Conference on Electronics Circuits and Systems (ICECS)* (2018), pp. 597–600.
8. M. Kiani and M. Ghovanloo, An RFID-based closed-loop wireless power transmission system for biomedical applications. *IEEE Transactions on Circuits and Systems II: Express Briefs* 57, 260 (2010).
9. Q. Shi, T. Wang, and C. Lee, MEMS based broadband piezoelectric ultrasonic energy harvester (PUEH) for enabling self-powered implantable biomedical devices. *Scientific Reports* 6, 24946 (2016).
10. T. Tokuda, T. Ishizu, W. Nattakarn, M. Haruta, T. Noda, K. Sasagawa, M. Sawan, and J. Ohta, 1 mm³-sized optical neural stimulator based on CMOS integrated photovoltaic power receiver. *AIP Advances* 8, 045018 (2018).
11. Y. J. Hung, M. S. Cai, J. F. Chen, H. W. Su, P. C. Jen, P. Chen, and T. C. Chang, High-voltage backside-illuminated CMOS photovoltaic module for powering implantable temperature sensors. *IEEE Journal of Photovoltaics* 8, 342 (2018).
12. E. Moon, D. Blaauw, and J. D. Phillips, Small-area Si photovoltaics for low-flux infrared energy harvesting. *IEEE Transactions on Electron Devices* 64, 15 (2017).
13. E. Moon, D. Blaauw, and J. D. Phillips, Subcutaneous photovoltaic infrared energy harvesting for bio-implantable devices. *IEEE Transactions on Electron Devices* 64, 2432 (2017).
14. Y. Hung Jr., T.-Y. Chuang, C.-L. Chun, M.-S. Cai, H.-W. Su, and S.-L. Lee, CMOS-enabled interdigitated back-contact solar cells for biomedical applications. *IEEE Transactions on Electron Devices* 61, 4019 (2014).
15. R.-F. Xue, K.-W. Cheng, and M. Je, High-efficiency wireless power transfer for biomedical implants by optimal resonant load transformation. *IEEE Transactions on Circuits and Systems I: Regular Papers* 60, 867 (2013).
16. Y. Guo, D. Zhu, and R. Jegadeesan, Inductive wireless power transmission for implantable devices, *2011 International Workshop on Antenna Technology (iWAT)* (2011), pp. 445–448.
17. D. Ahn and S. Hong, Wireless power transmission with self-regulated output voltage for biomedical implant. *IEEE Transactions on Industrial Electronics* 61, 2225 (2014).
18. J. Charthad, M. J. Weber, T. C. Chang, and A. Arbabian, A mm-sized implantable medical device (IMD) with ultrasonic power transfer and a hybrid bi-directional data link. *IEEE Journal of Solid-State Circuits* 50, 1741 (2015).
19. K. O. Htet, J. Zhao, R. Ghannam, and H. Heidari, Energy-efficient start-up power management for batteryless biomedical implant devices, *IEEE Int. Conference on Electronics, Circuits and Systems (ICECS)* (2018), pp. 597–600.
20. J. Zhao, R. Ghannam, Q. H. Abbasi, M. Imran, and H. Heidari, Simulation of photovoltaic cells for implantable sensory applications. *IEEE Sensors* (2018), pp. 1–4.
21. B. Shi, Z. Li, and Y. Fan, Implantable energy-harvesting devices. *Adv. Mater.* 30, 1801511 (2018).
22. E.-J. Yoon, J.-T. Park, and C.-G. Yu, Thermal energy harvesting circuit with maximum power point tracking control for self-powered sensor node applications. *Frontiers of Information Technology and Electronic Engineering* 19, 285 (2018).
23. K. Agarwal, R. Jegadeesan, Y.-X. Guo, and N. V. Thakor, Wireless power transfer strategies for implantable bioelectronics. *IEEE Reviews in Biomedical Engineering* 10, 136 (2017).
24. J. Chen, R. Ghannam, M. Imran, and H. Heidari, Wireless power transfer for 3D printed unmanned aerial vehicle (UAV) systems, *IEEE Asia Pacific Conf. on Postgraduate Research in Microelectronics and Electronics (PrimeAsia)* (2018), pp. 72–76.
25. M. Kiani and M. Ghovanloo, The circuit theory behind coupled-mode magnetic resonance-based wireless power transmission. *IEEE Transactions on Circuits and Systems I: Regular Papers* 59, 2065 (2012).
26. M. Schormans, V. Valente, and A. Demosthenous, Practical inductive link design for biomedical wireless power transfer: A tutorial. *IEEE Transactions on Biomedical Circuits and Systems* 12, 1112 (2018).
27. M. Kiani, U.-M. Jow, and M. Ghovanloo, Design and optimization of a 3-coil inductive link for efficient wireless power transmission. *IEEE Transactions on Biomedical Circuits and Systems* 99, 1 (2011).
28. C. Xiao, D. Cheng, and K. Wei, An LCC-C compensated wireless charging system for implantable cardiac pacemakers: Theory, experiment, and safety evaluation. *IEEE Transactions on Power Electronics* 33, 4894 (2018).
29. Z. Yang, W. Liu, and E. Basham, Inductor modeling in wireless links for implantable electronics. *IEEE Transactions on Magnetics* 43, 3851 (2007).
30. S. Li and C. C. Mi, Wireless power transfer for electric vehicle applications. *IEEE Journal of Emerging and Selected Topics in Power Electronics* 3, 4 (2015).
31. U.-M. Jow and M. Ghovanloo, Design and optimization of printed spiral coils for efficient transcutaneous inductive power transmission. *IEEE Transactions on Biomedical Circuits and Systems* 1, 193 (2007).
32. M. Kesler, Highly Resonant Wireless Power Transfer: Safe, Efficient, and Over Distance, Witricity Corporation (2013), pp. 1–32.
33. A. K. RamRakhyani, S. Mirabbasi, and M. Chiao, Design and optimization of resonance-based efficient wireless power delivery systems for biomedical implants. *IEEE Transactions on Biomedical Circuits and Systems* 5, 48 (2011).
34. F. Flack, E. James, and D. Schlapp, Mutual inductance of air-cored coils: Effect on design of radio-frequency coupled implants. *Medical and Biological Engineering* 9, 79 (1971).

Jinwei Zhao

Jinwei Zhao received a B.Eng. degree in Electrical and Electronics Engineering, University of Edinburgh, 2016 and received an M.Sc. degree in Electric Power, Newcastle University, UK, 2017. He is currently a Ph.D. student in University of Glasgow, from January 2018. The research interest is Energy harvesting, Implantable Systems and Solar cells.

Rami Ghannam

Rami Ghannam (B.Eng., DIC, M.Sc., Ph.D., MIET, SMIEEE) is a lecturer in Electronic and Electrical Engineering with research interests in the broad field of photonics. Following his Ph.D. from Cambridge University in 2007, Dr. Ghannam has spent the past ten years in the field of photovoltaics. He has held previous industrial appointments at Nortel Networks, IBM Research GmbH and Starkon S.A.E. He received his B.Eng. degree from King's College (top First-Class Honours), as well as his DIC and M.Sc. degrees from Imperial College London. Dr. Ghannam is also a member of the Microelectronics Lab, where he is investigating the use of PV cells for energy harvesting applications in wearable and implantable electronic device.

Mengyao Yuan

Mengyao Yuan received a B.Eng. degree in Electrical and Electronics Engineering, University of Glasgow College UESTC, 2018. She is currently studying the M.Sc. degree in Electrical and Electronics Engineering, University of Glasgow. The research interest is Energy harvesting for Implantable and Wearable Systems.

Himmy Tam

Himmy Tam received a B.Eng. Degree. In Electrical and Electronics Engineering, University of Glasgow, 2017. Currently studying the M.Sc. degree in Machine Learning in Imperial College London. The research interest is Robotics and deep learning.

Muhammad Imran

Muhammad Imran (B.Sc., M.Sc., DIC, Ph.D., CENG, FIET, SMIEEE) Fellow IET, Senior Member IEEE, Senior Fellow HEA is a Professor of Wireless Communication Systems with research interests in self organised networks, wireless networked control systems and the wireless sensor systems. He heads the Communications, Sensing and Imaging CSI research group at University of Glasgow. He is an Affiliate Professor at the University of Oklahoma, USA and a visiting Professor at 5G Innovation Centre, University of Surrey, UK. He has over 18 years of combined academic and industry experience with several leading roles in multi-million pounds funded projects. He has been awarded 15 patents; has authored/co-authored over 400 journal and conference publications; was editor of 2 books and author of more than 15 book chapters; has successfully supervised over 40 postgraduate students at Doctoral level. He has been a consultant to international projects and local companies in the area of self-organised networks.

Hadi Heidari

Hadi Heidari is a Lecturer (Assistant Professor) in the school of Engineering and head of the Microelectronics Lab (meLAB) at the University of Glasgow, UK. He has authored over 90 articles in peer reviewed journals (e.g., IEEE Solid-State Circuits and Systems I and IEEE Trans. Electron devices) and in international conferences. He has organised several conferences, workshops and special sessions, e.g., he is founder chairs of UK-China Emerging Technology (UCET) workshop, UK Circuits and Systems (UKCAS) workshop, and member of organising committee of SENSORS'17-'18, BioCAS'18, PRIME'19 and ICECS'20. He is an IEEE Senior Member, an Editor for the Elsevier Microelectronics Journal and lead Guest Editor for four journal special issues. He is member of the IEEE Circuits and Systems Society Board of Governors (BoG), IEEE Sensors Council and IEEE Solid-State Circuits Society Administrative Committee (AdCom). He has received several best paper awards from IEEE international conferences including ISCAS'14, PRIME'14, ISSCC'16, and travel scholarship from IEEE NGCAS'17. He has grant portfolio of £1 million funded by major research councils and funding organizations including European Commission, UK's EPSRC, Royal Society, Royal Academy of Engineering and Scottish Funding Council.

Copyright: American Scientific Publishers
Delivered by Ingenta